SANDIA REPORT
SAND2003–8246
Unlimited Release
Printed June 2003

Soot Properties and Species Measurements in a Two-Meter Diameter JP-8 Pool Fire

Jeffrey J. Murphy and Christopher R. Shaddix

Prepared by
Sandia National Laboratories
Albuquerque, New Mexico 87185 and Livermore, California 94550

Sandia is a multiprogram laboratory operated by Sandia Corporation,
a Lockheed Martin Company, for the United States Department of Energy's
National Nuclear Security Administration under Contract DE-AC04-94AL85000.

Sandia National Laboratories

Issued by Sandia National Laboratories, operated for the United States Department of Energy by Sandia Corporation.

Available to DOE and DOE contractors from
U.S. Department of Energy
Office of Scientific and Technical Information
P.O. Box 62
Oak Ridge, TN 37831

Telephone: (865)576-8401
Facsimile: (865)576-5728
E-Mail: reports@adonis.osti.gov
Online ordering: http://www.doe.gov/bridge

Available to the public from
U.S. Department of Commerce
National Technical Information Service
5285 Port Royal Rd
Springfield, VA 22161

Telephone: (800)553-6847
Facsimile: (703)605-6900
E-Mail: orders@ntis.fedworld.gov
Online order: http://www.ntis.gov/help/ordermethods.asp?loc=7-4-0#online

SAND2003–8246
Unlimited Release
Printed June 2003

Soot Properties and Species Measurements in a Two-Meter Diameter JP-8 Pool Fire

Jeffrey J. Murphy and Christopher R. Shaddix

Combustion Research Facility
Sandia National Laboratories
P.O. Box 969, Livermore, CA 94550

Abstract

A tunable diode laser absorption spectroscopy probe was used to measure in situ soot properties and species concentrations in two-meter diameter JP-8 pool fires. Twelve tests were performed at the Lurance Canyon Burn Site operated by Sandia in Albuquerque, New Mexico. Seven of the tests were conducted with the probe positioned close to the centerline at heights above the pool surface ranging from 0.5 m to 2.0 m in 0.25 m increments. For the remaining five tests, the probe was positioned at two heights 0.3 m from the centerline and at three heights 0.5 m from the centerline. Soot concentration was determined using a soot absorption measurement based on the transmission of a solid-state red laser (635 nm) through the 3.7 cm long probe volume. Soot temperature and a second estimate of soot concentration were measured using two-color optical pyrometry at 850 nm and 1000 nm. The effective data rate for these measurements was 10 kHz. Finally, tunable diode laser absorption spectroscopy was used to qualitatively estimate water concentration at a rate of 1 kHz. (To improve signal-to-noise, these data were averaged to an effective rate of 2 Hz.) The results presented include the statistics, probability density functions, and spectral density functions of soot concentration, soot temperature, and approximate water concentrations at the different measurement locations throughout the fire.

Acknowledgements

The authors would like to thank Tom Blanchat and the crew at the Luarance canyon burn site for providing the facilities and supporting the experiments detailed in this report. We would also like to thank Lyle Pickett and Alex Brown for a thorough review of the manuscript. Alan Kerstein provided helpful suggestions regarding the interpretation of the power spectral density functions.

Contents

List of Figures

List of Tables

Nomenclature

a	line strength
C_1	first radiation constant = $3.741\,771 \times 10^{-16}$ W m^2
C_2	second radiation constant = $1.438\,775 \times 10^{-2}$ m K
d	particle diameter [nm]
f	arbitrary dependent variable
f_v	soot volume fraction [ppm]
I	intensity [W/m^2]
K	dimensionless soot extinction coefficient = $k\lambda/f_v$
k	soot extinction coefficient [m^{-1}]
N	total number of independent variables
p	pressure [Pa]
s	path length [m]
T	temperature [K]
V	voltage [V]
$\tilde{V}$	normalized voltage = V/V_{ref}
x	arbitrary independent variable

Greek symbols

δf	measurement uncertainty in f
Δf	indicates a difference between two values of f
ε	emissivity
λ	wavelength [nm]
π	3.141 593...
ρ	correlation coefficient of two error sources
σ	line strength temperature dependence

Subscripts

0	initial
a	absorption
b	blackbody
e	emission or extinction
i	index
j	index
ref	reference value
t	transmission
λ	spectral quantity

Introduction

Researchers at Sandia National Laboratories have been investigating large-scale pool fires, both experimentally and numerically, for several years, because of the risk that these fires pose to critical engineered systems during transport accident scenarios. In order to develop and validate high-fidelity computational models of fires, with an emphasis on heat transfer to imbedded or nearby objects, temporally and spatially resolved information on the scalar fields within these fires is needed.

In particular, knowledge of the soot concentration and soot temperature fields within these fires is required to quantify heat transfer, since it is dominated by high-temperature soot emission. Diagnostics with high frequency responses are needed to provide information about the small-scale turbulence structure. Measurements of the chemical fields within large fires are practically nonexistent, and therefore there is little information about the effects of gas-phase emission and absorption on the overall radiant transport within and away from fires. Also, the extent of mixing as a function of radial distance in large fires has not been quantified, nor have the concentrations of gas species responsible for soot formation, growth, and oxidation been measured.

Some of these issues were addressed in a recent study [1], where Sandia fielded a multi-wavelength absorption / emission diagnostic to make the first in situ measurements of soot properties in a large (6 m by 6 m) JP-8 pool fire. However, data presented were only at one position and had limited bandwidth (100 Hz). The diagnostic was based on one used by Gore and co-workers to make similar measurements in laboratory-scale flames [2,3].

To further address the issues outlined above, Sandia developed a capability for performing multiple-species, fiber-coupled, near-infrared tunable diode laser absorption spectroscopy in large fires, with concurrent soot absorption and emission measurements [4]. The optics are contained in a horseshoe-shaped, insulated, water-jacketed, aluminum probe suspended in the fire; the probe is similar to that used in Ref. 1. Here, we utilize this new probe to make spatially and temporally resolved measurements in a two-meter diameter JP-8 pool fire in Sandia's enclosed pool-fire facility.

Description of Diagnostics

Species Measurement

Tunable diode laser absorption spectroscopy (TDLAS) was performed in this series of tests to detect two species: H_2O and C_2H_2. To obtain the required sensitivity, we use a Herriott cell configuration with one-inch mirrors at a set spacing allowing eighteen optical passes across the 36.5 mm × 1.5 cm dia. cylindrical probe volume. The TDLs are multiplexed together and transmitted through a common optical path. The driving signals for the TDLs consist of a high-frequency (~1 MHz) modulation superimposed upon a low-frequency (1 kHz) ramp. The high frequencies are varied for the individual lasers so that they can be de-multiplexed by using separate lock-in amplifiers for each frequency (frequency-division

multiplexing). The data acquisition and TDL hardware allow one spectral scan, 114 points in length and nominally 0.15 nm in spectral width, for each channel every millisecond.

The TDL waveforms were ensemble-averaged to improve signal to noise and were normalized by the average value of the 0f signal [5]. Then the magnitude a of the 2f absorption peak was measured. To determine species partial pressure from line strength, the measurement must be corrected for the effects of temperature on the line strength and the density.

$$p_i = \frac{p_{ref}}{\sigma(T)} \frac{a}{a_{ref}} \frac{T}{T_{ref}} \frac{s_{ref}}{s} \tag{1}$$

Here, $\sigma(T)$ is line strength as a function of temperature normalized by the line strength at the reference temperature, and can be either calculated using the HITRAN and HITEMP molecular spectroscopy databases [6,7], or determined from experimental measurements reported in the literature. Density effects are corrected by scaling the line strength with a reference cell line strength a_{ref} measured at temperature T_{ref} and partial pressure of p_{ref} measured in a cell with a path length of s_{ref}. This correction uses the soot temperature with the assumption that the species under consideration is in thermal equilibrium with the soot. Additionally, the modulation of the laser couples nonlinearly with the linewidth to change measured line strength. Transitions that exhibit significant changes in linewidth with temperature are affected. This effect is not considered here.

In this series of tests, several problems with the TDLAS system, including intermittent noise, difficulties setting the phase on the lock-in amplifiers, and insufficient detector gain, resulted in unusable C_2H_2 data. To deal with the noise problem, the H_2O data had to be ensemble-averaged in half-second bins. Thus, only limited species data are presented in this report.

The H_2O absorption measurement was made using an overtone transition at 1309.68 nm (ν'–ν'' = 000–002, ϕ'–ϕ'' = 4,3,2–5,4,1). This transition was characterized recently by Upschulte and Allen [8]. Their data, consisting of measurements of H_2O line strength as a function of temperature up to 1100 K, show significant differences from predictions using the HITEMP database. We thus use their measurements to form an approximate linear relation to correct for the effects of temperature on line strength. This relation, shown in Fig. 1, is $\sigma(T) = 1.41 - 0.69(T/1000\ \mathrm{K})$.

Although our H_2O measurements are corrected for temperature effects, the calibration was not quantitative because the water concentration within the reference cell was unknown. Due to this issue, as well as the limited amount of data and the unquantified coupling of linewidth changes and the laser modulation, the uncertainty in the presented species measurements has not been determined.

Soot Measurement

A visible laser absorption/soot emission diagnostic similar to that used in the previous experiments at Sandia [1] was incorporated into the probe. A 9 μm single-mode fiber is used to transport light to the probe volume for the transmission measurement. The laser light

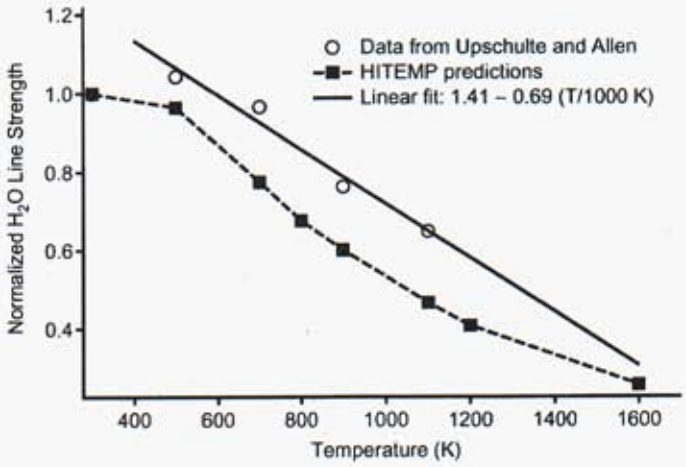

Figure 1. Comparison of measurements of water vapor line strength by Upschulte and Allen to predictions using the HITEMP database. The linear fit is used to correct the measured line strength for the effects of temperature.

is collimated with a 4.6 mm aspherical lens and then projected across the probe volume. The light is then collected via a 5.5 mm diameter aspherical lens onto a 62.5 μm solid-core multimode fiber and transmitted back to the equipment trailer. The combination of the 9 μm delivery fiber and the 62.5 μm receiving fiber is insensitive to beam steering. The lenses are mounted behind the TDL Herriott cell mirrors, and use centerline holes drilled through the mirrors for optical access to the probe volume.

The laser source is a directly modulated 635 nm diode laser. We impose a sinusoidal modulation at high frequency (50 kHz) and then use an analog lock-in amplifier with a time constant of 100 μs to provide a measurement of the transmitted laser power that is completely insensitive to thermal emission or any other light sources. The combination of the modulated laser and the narrow field of view of the fiber optic ensures that this is a true extinction measurement. A low-pass spectral filter is used to clean up the output of the diode laser and a laser-line notch filter further rejects any competing light sources incident upon the reference or signal diode detectors.

A dichroic beamsplitter is used at the output end of the receiving fiber to separate the near-infrared wavelengths from the transmission measurement laser signal. Silicon avalanche photodiodes (APDs), with 5 kHz bandwidths and 3 mm diameter active areas, are used to detect the thermal emission signals through near-IR bandpass filters. The transmissivity and emission data were recorded at 114 kHz. During post-processing, the data were averaged to give an effective sample rate of 10 kHz.

The emission measurement was calibrated with a blackbody source (emissivity 0.97–0.98) overfilling the collection optics. The source was aimed into the head end of the probe with a silver mirror (reflectivity 0.98–0.99). A multi-point calibration was performed from 1200–1700 °C using a neutral density filter with optical density of 1.0 (10% transmittance).

The resulting effective emissivity of the source was 0.096.

The TDLAS power supply was used to power the emission-measurement APDs. As a result, the power spectra of the emission measurements have strong peaks at 120 Hz and higher harmonics, presumably from the same noise source that affected the TDLAS measurement. This noise problem will be addressed for the next set of measurements.

Theory of the Soot Absorption / Emission Diagnostic

From the 635 nm transmissivity measurement, the soot extinction coefficient in the probe volume is determined:

$$k_{e,\lambda} \equiv \frac{K_{e,\lambda} f_{v,l}}{\lambda} = -\frac{1}{s} \ln\left(\frac{I_\lambda}{I_{\lambda,0}}\right) \tag{2}$$

Here, $I_\lambda / I_{\lambda,0}$ is the measured transmissivity and s is the path length. This equation is a version of the transmissivity function defined on page 233 of Brewster [9], and is strictly valid only for a homogeneous medium. As applied to our measurement, $k_{e,\lambda}$ is a mean extinction coefficient corresponding to a mean soot volume fraction, that is

$$k_{e,\lambda} = \frac{1}{s}\int_0^s k'_{e,\lambda}\,\mathrm{d}s' = \frac{K_{e,\lambda} f_{v,l}}{\lambda} = \frac{1}{\lambda s}\int_0^s K'_{e,\lambda} f'_{v,l}\,\mathrm{d}s' \tag{3}$$

Utilizing an estimate of the mean dimensionless spectral extinction coefficient $K_{e,\lambda}$, the mean soot volume fraction is determined from the measurement using

$$f_{v,l} = -\frac{\lambda}{K_{e,\lambda} s} \ln\left(\frac{I_\lambda}{I_{\lambda,0}}\right) \tag{4}$$

where λ is the laser wavelength.

Soot temperature is determined from soot emission intensity, which is in turn governed by Planck's black-body radiation law (see page 9 of Ref. 9):

$$I_{b,\lambda}(T) = \frac{C_1/\pi}{\lambda^5 \left(\mathrm{e}^{C_2/\lambda T} - 1\right)} \tag{5}$$

Here, λ is the emission wavelength. After calibration with a reference source of emissivity $\varepsilon_{\mathrm{ref}}$ and temperature T_{ref}, the voltage output V_λ of the detector, which is proportional to the detected intensity, is

$$\frac{V_\lambda}{V_{\lambda,\mathrm{ref}}} = \frac{\varepsilon_\lambda}{\varepsilon_{\mathrm{ref}}} \frac{\mathrm{e}^{C_2/\lambda T_{\mathrm{ref}}} - 1}{\mathrm{e}^{C_2/\lambda T} - 1} \tag{6}$$

Emission is measured at two wavelengths, 850 nm and 1000 nm. Using the typical expression for emissivity due to soot, $\varepsilon_\lambda = (1 - \mathrm{e}^{-K_{a,\lambda} f_{v,l} s/\lambda})$ (see Ref. 10), we have two equations and two unknowns which can be solved for temperature and soot volume fraction simultaneously. Note that the emission-derived temperature is dependent on the ratio of the emissivities at the two detection wavelengths, whereas the emission-derived soot volume fraction is dependent on the absolute values of the emissivities.

Optical Constants for Soot

It has been a tradition within the fire community to use the dispersion relations proposed by Dalzell and Sarofim [11] to calculate optical constants for interpreting soot measurements in pool fires. These relations give a value for K_a of 4.87 at 632 nm, and values of 5.20 and 5.47 at 850 nm and 1000 nm, respectively. Because of the wide range of refractive index values measured for soot in different flame systems [12], these constants generally have high uncertainty, limiting the accuracy of the measurements. Some studies have attempted to circumvented this issue by making extinction and emission measurements simultaneously at the operative wavelengths [13–15].

In both cases, the assumption is made that the Rayleigh limit of Mie theory accurately describes the absorption and scattering of the soot. This assumption is usually justified by noting that the dimensionless size parameter from Mie theory, $\pi d/\lambda$, is much less than one for typical primary soot particles ($d \approx$ 10–50 nm). If particle sizes are measured as part of the experiment, these are sometimes checked for consistency with the Rayleigh approximation. Otherwise, there is usually no check on the validity of the Rayleigh-limit assumption.

As a result of this assumption, scattering is assumed to be negligible. Thus, soot extinction is equated with soot absorption and the respective coefficients can be used interchangeably in the equations for deducing soot temperature and volume fraction. However, recent measurements of soot scattering [16–18] indicate that soot *does not* behave like a Rayleigh scatterer, even in the near-infrared. Indeed, a recent study reported measurements of soot scattering to extinction ratios range from 18–25% for acetylene- and ethene-air flames [19]. Thus, contrary to the Rayleigh limit approximations, scattering makes a significant contribution to radiation extinction by soot, and the absorption and extinction coefficients cannot be used interchangeably. For emission measurements in fires, in-scattering from the soot surrounding the probe volume is a confounding factor that in general is not easily accounted for.

With certain geometries, the body of the probe can act as a radiation shield for the probe volume. The forward-scattering nature of soot can then be exploited to derive an absorption-based expression for soot emissivity, $\varepsilon_\lambda = 1 - e^{-K_{a,\lambda} f_v L}$ [10]. Although this expression is identical to that used in the literature for soot emission measurements, the assumptions underlying the derivation are different. Notably, instead of assuming that there is no scattering, one assumes that out-scattering is exactly balanced by in-scattering.

If all of the radiation from optically thick surroundings reaches the probe volume, the result is another limiting case for soot emissivity: $\varepsilon_\lambda = 1 - e^{-K_{e,\lambda} f_v L}$. This expression can perhaps be considered an upper-bound on measured emissivity. However, this interpretation does not strictly hold, since the expression was derived for a homogeneous medium and fires are typically very heterogeneous on the scale of many optical path lengths.

In this study, we assume that $K_{e,\lambda,\,635\,\mathrm{nm}} = 8.0$, a value measured in identical two-meter JP-8 pool fires using extractive sampling and a transmission-cell reciprocal nephelometer (TCRN) [20]. (For a description of a TCRN similar to the one used in these measurements, see Ref. 21.) This value of $K_{e,\lambda}$ is also consistent with recent determinations for post-flame

soot when burning a variety of fuels in various flames [18,22]. For the emission measurement, we assume $K_{a,\lambda=850\text{nm}} = K_{a,\lambda=1000\text{nm}} = 6.0$. This value was estimated from the previously mentioned measurements [20] and an assumption that $K_{a,\lambda}/K_{e,\lambda} \approx 0.75$, consistent with the recent measurements in acetylene-air flames [19,22]. The probe used in this study has a geometry that shields the probe volume from much of the surrounding radiation. Thus, it is appropriate to use K_a rather than K_e in the soot emissivity expression.

Measurement Uncertainty

The effects of various operating parameters on the soot absorption / emission diagnostic are discussed in Ref. 1. An extensive sensitivity analysis of the two-color optical pyrometry technique as applied to soot measurements has been published by di Stasio and Massoli [23]. Here, we use first-order propagation of uncertainty combined with estimates of instrumentation noise to determine the uncertainty in our soot measurements.

Given an experimental measurement f that is a function of the parameters $x_1, x_2, \ldots$ (measured or otherwise), the first-order uncertainty in the measurement of f is given by (see Ref. 24)

$$\left(\frac{\delta f}{f}\right)^2 = \sum_{i=1}^{N}\left(\frac{x_i}{f}\frac{\partial f}{\partial x_i}\frac{\delta x_i}{x_i}\right)^2 + 2\sum_{i=1}^{N-1}\sum_{j=i+1}^{N}\rho_{x_i x_j}\frac{x_i}{f}\frac{\partial f}{\partial x_i}\frac{x_j}{f}\frac{\partial f}{\partial x_j}\frac{\delta x_i}{x_i}\frac{\delta x_j}{x_j} \tag{7}$$

The uncertainty δf is taken to be twice the standard deviation of f (i.e. $2\sigma_f$). Thus, δf roughly corresponds to a 95% confidence interval. The correlation coefficient, $\rho_{x_i x_j}$, is the covariance of the uncertainties in x_i and x_j normalized by the uncertainties in x_i and x_j (i.e. $\rho_{x_i x_j} = \delta(x_i x_j)/\delta x_i \delta x_j$).

Transmission Measurement The measurement of the soot extinction coefficient, $k_{e,\lambda}$, is based on a direct laser transmissivity measurement, $I_\lambda/I_{\lambda,0}$, over a path of length s. Referring to Eq. 2, $k_{e,\lambda} = -\ln(I_\lambda/I_{\lambda,0})/s$, and assuming that the different variables are uncorrelated, the application of Eq. 7 is straightforward:

$$\left(\frac{\delta k_{e,\lambda}}{k_{e,\lambda}}\right)^2 = \left(\frac{\delta(I_\lambda/I_{\lambda,0})/(I_\lambda/I_{\lambda,0})}{k_{e,\lambda}s}\right)^2 + \left(\frac{\delta s}{s}\right)^2 \tag{8}$$

Soot volume fraction is determined from the extinction coefficient, a dimensionless coefficient K_e, and the wavelength of the laser: $f_{v,l} = k_{e,\lambda}\lambda/K_{e,\lambda}$. (In our experiments, $\lambda =$ 635 nm.) Thus,

$$\left(\frac{\delta f_{v,l}}{f_{v,l}}\right)^2 = \left(\frac{\delta k_{e,\lambda}}{k_{e,\lambda}}\right)^2 + \left(\frac{\delta K_{e,\lambda}}{K_{e,\lambda}}\right)^2 = \left(\frac{\delta(I_\lambda/I_{\lambda,0})/(I_\lambda/I_{\lambda,0})}{k_{e,\lambda}s}\right)^2 + \left(\frac{\delta s}{s}\right)^2 + \left(\frac{\delta K_{e,\lambda}}{K_{e,\lambda}}\right)^2 \tag{9}$$

Emission Measurement The equation for calculating soot emissivity based on the measurement of signal V_{λ_i} from the avalanche photodiode (APD) detector referenced to a calibration voltage V_{ref,λ_i}:

$$\varepsilon_{\lambda_i} = 1 - \exp\left(-\frac{K_{a,\lambda_i} f_{v,e} s}{\lambda_i}\right) = \tilde{V}_i \exp\left[\frac{C_2}{\lambda_i}\left(\frac{1}{T_e} - \frac{1}{T_{ref}}\right)\right] \tag{10}$$

Here, we measure soot emission temperature, T_e, and soot volume fraction, $f_{v,e}$, based on the values of K_{a,λ_i}, s, and $\tilde{V}_i = V_{\lambda_i}/V_{ref,\lambda_i}$. The parameters λ_i and T_{ref} are deterministic inputs into the calibration procedure, and thus have no uncertainty associated with them. The uncertainty of the radiation constant C_2 is negligible; $\delta C_2/C_2 = 3.4 \times 10^{-6}$ [25].

We take the derivative and divide through by original equation:

$$\frac{1-\varepsilon_{\lambda_i}}{\varepsilon_{\lambda_i}} \frac{K_{a,\lambda_i} f_{v,e} s}{\lambda_i} \left(\frac{\mathrm{d}K_{a,\lambda_i}}{K_{a,\lambda_i}} + \frac{\mathrm{d}f_{v,e}}{f_{v,e}} + \frac{\mathrm{d}s}{s}\right) = \frac{\mathrm{d}\tilde{V}_i}{\tilde{V}_i} - \frac{C_2}{\lambda_i T_e} \frac{\mathrm{d}T_e}{T_e} \tag{11}$$

Soot Volume Fraction The emission measurement is made at two wavelengths, λ_1 and λ_2. We thus have two versions of Eq. 11 which we combine to determine the two unknowns, $f_{v,e}$ and T_e. We now combine those equations to eliminate $\mathrm{d}T_e$:

$$\left(K_{a,\lambda_1} \frac{1-\varepsilon_{\lambda_1}}{\varepsilon_{\lambda_1}} - K_{a,\lambda_2} \frac{1-\varepsilon_{\lambda_2}}{\varepsilon_{\lambda_2}}\right)\left(\frac{\mathrm{d}f_{v,e}}{f_{v,e}} + \frac{\mathrm{d}s}{s}\right) = \frac{\lambda_1}{f_{v,e} s} \frac{\mathrm{d}\tilde{V}_1}{\tilde{V}_1} - \frac{\lambda_2}{f_{v,e} s} \frac{\mathrm{d}\tilde{V}_2}{\tilde{V}_2} - \frac{1-\varepsilon_{\lambda_1}}{\varepsilon_{\lambda_1}} \mathrm{d}K_{a,\lambda_1} + \frac{1-\varepsilon_{\lambda_2}}{\varepsilon_{\lambda_2}} \mathrm{d}K_{a,\lambda_2} \tag{12}$$

We now make a modification to the treatment of the optical constants. The uncertainties in K_{a,λ_1} and K_{a,λ_2} are very large, but the uncertainty in the difference, $K_{a,\lambda_1} - K_{a,\lambda_2}$, is much smaller. In other words, the uncertainties in K_{a,λ_1} and K_{a,λ_2} are highly correlated. Rather than trying to determine a suitable correlation coefficient for these two variables, we rewrite them in terms of two uncorrelated variables K_a and ΔK_a: $K_{a,\lambda_1} = K_a - \Delta K_a$ and $K_{a,\lambda_2} = K_a + \Delta K_a$. This will make the subsequent analysis easier and more intuitive.

$$K_a\left(\frac{1-\varepsilon_{\lambda_1}}{\varepsilon_{\lambda_1}} - \frac{1-\varepsilon_{\lambda_2}}{\varepsilon_{\lambda_2}}\right)\left(\frac{\mathrm{d}f_{v,e}}{f_{v,e}} + \frac{\mathrm{d}s}{s}\right) = \frac{\lambda_1}{f_{v,e} s} \frac{\mathrm{d}\tilde{V}_1}{\tilde{V}_1} - \frac{\lambda_2}{f_{v,e} s} \frac{\mathrm{d}\tilde{V}_2}{\tilde{V}_2} - \left(\frac{1-\varepsilon_{\lambda_1}}{\varepsilon_{\lambda_1}} - \frac{1-\varepsilon_{\lambda_2}}{\varepsilon_{\lambda_2}}\right)\mathrm{d}K_a + \left(\frac{1-\varepsilon_{\lambda_1}}{\varepsilon_{\lambda_1}} + \frac{1-\varepsilon_{\lambda_2}}{\varepsilon_{\lambda_2}}\right)\mathrm{d}\Delta K_a \tag{13}$$

Now, using the above equation, we calculate the sensitivity coefficients:

$$\frac{\tilde{V}_1}{f_{v,e}} \frac{\partial f_{v,e}}{\partial \tilde{V}_1} = \frac{\lambda_1/(K_a f_{v,e} s)}{(1-\varepsilon_{\lambda_1})/\varepsilon_{\lambda_1} - (1-\varepsilon_{\lambda_2})/\varepsilon_{\lambda_2}} \tag{14}$$

$$\frac{\tilde{V}_2}{f_{v,e}} \frac{\partial f_{v,e}}{\partial \tilde{V}_2} = -\frac{\lambda_2/(K_a f_{v,e} s)}{(1-\varepsilon_{\lambda_1})/\varepsilon_{\lambda_1} - (1-\varepsilon_{\lambda_2})/\varepsilon_{\lambda_2}} \tag{15}$$

$$\frac{K_a}{f_{v,e}}\frac{\partial f_{v,e}}{\partial \Delta K_a} = \frac{(1-\varepsilon_{\lambda_1})/\varepsilon_{\lambda_1} + (1-\varepsilon_{\lambda_2})/\varepsilon_{\lambda_2}}{(1-\varepsilon_{\lambda_1})/\varepsilon_{\lambda_1} - (1-\varepsilon_{\lambda_2})/\varepsilon_{\lambda_2}} \tag{16}$$

$$\frac{K_a}{f_{v,e}}\frac{\partial f_{v,e}}{\partial K_a} = \frac{s}{f_{v,e}}\frac{\partial f_{v,e}}{\partial s} = -1 \tag{17}$$

We now substitute these coefficients back into Eq. 7 to get an expression for the uncertainty of soot volume fraction. We assume that the instrument uncertainties in the APDs are equal, and thus let $\delta\tilde{V}_1/\tilde{V}_1 = \delta\tilde{V}_2/\tilde{V}_2 = \delta\tilde{V}/\tilde{V}$. We also assume that all dependent variables are uncorrelated, except for the detector signals $\tilde{V}_1$ and $\tilde{V}_2$.

$$\left(\frac{\delta f_{v,e}}{f_{v,e}}\right)^2 = \frac{\lambda_1^2 + \lambda_2^2 - 2\rho_{V_1V_2}\lambda_1\lambda_2}{(K_a f_{v,e} s)^2\left[(1-\varepsilon_{\lambda_1})/\varepsilon_{\lambda_1} - (1-\varepsilon_{\lambda_2})/\varepsilon_{\lambda_2}\right]^2}\left(\frac{\delta\tilde{V}}{\tilde{V}}\right)^2 + \left(\frac{\delta K_a}{K_a}\right)^2 + \left(\frac{(1-\varepsilon_{\lambda_1})/\varepsilon_{\lambda_1} + (1-\varepsilon_{\lambda_2})/\varepsilon_{\lambda_2}}{(1-\varepsilon_{\lambda_1})/\varepsilon_{\lambda_1} - (1-\varepsilon_{\lambda_2})/\varepsilon_{\lambda_2}}\right)^2\left(\frac{\delta\Delta K_a}{K_a}\right)^2 + \left(\frac{\delta s}{s}\right)^2 \tag{18}$$

Temperature Here, we proceed the same as above, except we eliminate $\mathrm{d}f_{v,e}$ from the combination of Eq. 11 rather than $\mathrm{d}T_e$.

$$\left[\frac{\varepsilon_{\lambda_2}}{1-\varepsilon_{\lambda_2}} - \frac{\varepsilon_{\lambda_1}}{1-\varepsilon_{\lambda_1}}\right]\frac{C_2}{T_e}\frac{\mathrm{d}T_e}{T_e} = \lambda_2\frac{\varepsilon_{\lambda_2}}{1-\varepsilon_{\lambda_2}}\frac{\mathrm{d}\tilde{V}_2}{\tilde{V}_2} - \lambda_1\frac{\varepsilon_{\lambda_1}}{1-\varepsilon_{\lambda_1}}\frac{\mathrm{d}\tilde{V}_1}{\tilde{V}_1} - 2 f_{v,e} s\,\mathrm{d}\Delta K_a \tag{19}$$

The sensitivity coefficients are

$$\frac{V_1}{T_e}\frac{\partial T_e}{\partial V_1} = -\frac{T_e}{C_2}\frac{\lambda_1\varepsilon_{\lambda_1}/(1-\varepsilon_{\lambda_1})}{\varepsilon_{\lambda_2}/(1-\varepsilon_{\lambda_2}) - \varepsilon_{\lambda_1}/(1-\varepsilon_{\lambda_1})} \tag{20}$$

$$\frac{V_2}{T_e}\frac{\partial T_e}{\partial V_2} = \frac{T_e}{C_2}\frac{\lambda_2\varepsilon_{\lambda_2}/(1-\varepsilon_{\lambda_2})}{\varepsilon_{\lambda_2}/(1-\varepsilon_{\lambda_2}) - \varepsilon_{\lambda_1}/(1-\varepsilon_{\lambda_1})} \tag{21}$$

$$\frac{K_a}{T_e}\frac{\partial T_e}{\partial \Delta K_a} = -\frac{T_e}{C_2}\frac{2K_a f_{v,e} s}{\varepsilon_{\lambda_2}/(1-\varepsilon_{\lambda_2}) - \varepsilon_{\lambda_1}/(1-\varepsilon_{\lambda_1})} \tag{22}$$

$$\frac{K_a}{T_e}\frac{\partial T_e}{\partial K_a} = \frac{s}{T_e}\frac{\partial T_e}{\partial s} = 0 \tag{23}$$

Once again, we substitute these coefficients into Eq. 7 to get

$$\left(\frac{\delta T_e}{T_e}\right)^2 = \frac{T_e/C_2}{\varepsilon_{\lambda_1}/(1-\varepsilon_{\lambda_1}) - \varepsilon_{\lambda_2}/(1-\varepsilon_{\lambda_2})}\left\{(2 f_{v,e} s\,\delta\Delta K_a)^2 + \left[\left(\frac{\lambda_1\varepsilon_{\lambda_1}}{1-\varepsilon_{\lambda_1}}\right)^2 + \left(\frac{\lambda_2\varepsilon_{\lambda_2}}{1-\varepsilon_{\lambda_2}}\right)^2 - 2\rho_{V_1V_2}\left(\frac{\lambda_1\varepsilon_{\lambda_1}}{1-\varepsilon_{\lambda_1}}\frac{\lambda_2\varepsilon_{\lambda_2}}{1-\varepsilon_{\lambda_2}}\right)\right]\left(\frac{\delta\tilde{V}}{\tilde{V}}\right)^2\right\} \tag{24}$$

		Uncertainty (%)		
Source	Symbol	src	$k_{e,\lambda}$	$f_{v,t}$
Diode detector	$I_\lambda/I_{\lambda,0}$	2	4	4
Extinction coefficient	$K_{e,\lambda}$	10	0	10
Path length	s	5	5	5
		Total:	7	12

Table 1. Transmission measurement uncertainties. The total uncertainties for $k_{e,\lambda}$ and $f_{v,t}$ are calculated from Eqs. 8 and 9, respectively. The contributions of the different sources of uncertainty correspond to the contributions of the different terms in Eqs. 8 and 9.

		Uncertainty (%)		
Source	Symbol	src	$f_{v,e}$	T_e
APD detectors	$\tilde{V}$	4	16	1
Absorption coefficient	K_a	20	20	0
	ΔK_a	3	33	3
Path length	s	5	5	0
		Total:	42	3

Table 2. Emission measurement uncertainties. The total uncertainties for $f_{v,e}$ and T_e are calculated from Eqs. 18 and 24, respectively. The contributions of the different sources of uncertainty correspond to the contributions of the different terms in Eqs. 18 and 24.

Uncertainty Results To estimate uncertainties for the present data set, we assumed a nominal soot volume fraction of 1.0 ppm and a nominal soot temperature of 1400 K. The wavelengths of the emission measurement were $\lambda_1 = 850$ nm and $\lambda_2 = 1000$ nm. Values of the optical constants are the same as those used in the rest of the paper, $K_a = 6.0$ and $K_{e,\lambda=635\text{ nm}} = 8.0$. The path length s is 36.5 mm.

Uncertainty in the extinction coefficient measurement is expected to be low, as it is based on a direct transmission measurement. We estimate the uncertainty in the transmissivity $I_\lambda/I_{\lambda,0}$ to be $\pm 2\%$ from baseline measurements with no flames. The extinction coefficient k_e is 12.6 m^{-1}, resulting in a sensitivity coefficient of approximately 2. The uncertainty in the path length is larger, estimated at ± 2.0 mm ($\pm 5\%$). Thus, the overall uncertainty in the extinction coefficient measurement is $\pm 7\%$. Assuming a $\pm 10\%$ uncertainty in K_e, the resulting uncertainty in soot volume fraction from the transmission measurement is $\pm 12\%$. A breakdown of these results is shown in Table 1. Several laboratory experiments were conducted using non-sooting flames to measure the effect of beam-steering on the diagnostic. The results indicated that beamsteering was a negligible source of uncertainty (<1%).

For the emission measurement, using the parameter values above, we find $\varepsilon_{\lambda_1} = 0.23$

and $\varepsilon_{\lambda_2} = 0.20$. The uncertainty in the APD measurement, $\delta\tilde{V}/\tilde{V}$, was estimated to be $\pm 4\%$ from the blackbody calibration data. This number includes all instrument noise ($\pm 3\%$), as well as calibration uncertainties ($\pm 2\%$). The correlation coefficient, $\rho_{\lambda_1\lambda_2}$, was also estimated from these data; it has a value of 0.8. This high correlation suggests that the majority of the noise in the APD detector signals is from a common source, such as the power supply.

The uncertainty in the mean value of the absorption coefficient, $\delta K_a/K_a$, was given a value of $\pm 20\%$. The uncertainty in the difference in the two absorption coefficients, $\delta\Delta K_a/K_a$, was assigned a value of $\pm 3\%$. This number comes from the Dalzell and Sarofim values for the optical constants (5.20 and 5.47 at 850 nm and 1000 nm, respectively), for which $\Delta K_a/K_a = 2.5\%$.

Using these values and the $\pm 5\%$ uncertainty in the path length, we find the total uncertainty of $f_{v,e}$ to be $\pm 42\%$. For temperature, using the values of the parameters above, we find an uncertainty of $\pm 3\%$, or ± 40 K. The results are summarized in Table 2. Taking into account these uncertainties and the characteristics of the APD detectors, we estimate the detection limit for soot temperature to be about 800 K.

Due to a desire to map out as much of the fire as possible with limited time and budget, no repeat tests were performed in this test series. However, the tests on the centerline were interleaved. Thus, the consistency of the trends seen in the data serves as an indicator of the repeatability of these measurements. Repeat tests at the same location are planned for the next series of experiments.

Probe Volume Heterogeneity Previous studies [1,26] have noted that heterogeneous soot populations, where soot temperature and/or soot volume fraction vary significantly across the probe volume, will tend to bias the emission measurements towards the hottest soot. In other words, temperature and soot volume fraction deduced from emission measurements will tend to reflect the temperature and soot volume fraction of the hottest soot in the probe volume, rather than the average temperature and soot volume fraction of all soot in the probe volume. This bias occurs because the hot soot is emitting much more strongly than the cool soot. To examine the effects of heterogeneity on our measurements, we used the equations from page 12 to simulate an extreme, idealized case of probe volume heterogeneity.

We assume that the probe volume has two soot populations, one cold (1200 K) and one hot (1800 K). Both populations have soot concentrations of 2 ppm. The populations are layered, perpendicular to the axis of the collection optics, in a probe volume with a path length of 36.5 mm. The results of the calculations are shown in Fig. 2.

The measured temperature of the soot layers depends on the temperature of the soot layer closest to the collection optics. Cold soot adjacent to the optics will absorb some of the emission from the hot soot, resulting in a lower measured temperature relative to the opposite case. In both cases, however, the measured temperature is within 150 K of the hot soot temperature when there is more than 20% hot soot in the probe volume. The emission soot volume fraction measurement is even more biased; its value approximately corresponds to the volume fraction of the hot soot (as opposed to all of the soot) in the probe volume when there is more than 5% hot soot.

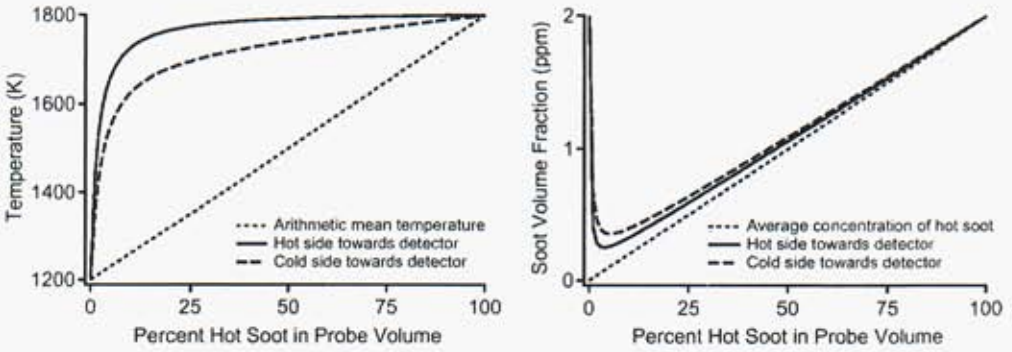

Figure 2. Comparison of the computed and average emission temperature and emission soot volume fraction in a heterogeneous probe volume.

While the calculations performed here represent an extreme case of soot heterogeneity, the results shown in Fig. 2 demonstrate that the two-color emission technique is strongly biased towards the hot soot component of a heterogeneous probe volume. Hence, the measurement is always biased high in temperature and low in soot volume fraction when heterogeneous conditions exist. Future testing will use several different probe volume lengths to further evaluate the impact of this phenomenon on the measured soot properties.

Summary of Experiments Performed

A series of tests was conducted in August 2002 at Sandia's FLAME (Fire Laboratory for Accreditation of Modeling by Experiment) facility at the Lurance Canyon Burn Site near Albuquerque, New Mexico. This facility is fully described in Refs. 27 and 28; a brief description is given here.

JP-8 fuel was floated in a 2 m diameter pan on a layer of water nominally 10.0 cm deep. 38 L (10 gal) of JP-8 were used for each test, giving a layer of JP-8 approximately 1.2 cm thick. The water was either replaced or allowed to cool substantially after each test to assure uniform boundary conditions. Air was injected into a honeycomb ring on the floor 1.8 m below the bottom of the pan. The temperatures of the fuel, water, and air were monitored with thermocouples during the tests, and the instantaneous fuel depth was monitored with a differential-pressure transducer. The fuel regression rate was calculated by applying a linear regression to the fuel depth data over the time interval of the analysis. The specific gravity of the fuel was assumed to be 0.8 [29].

The measurement probe is fully described in Ref. 4. The outer skin of the probe was fashioned from 8.9 cm (3.5 in) square aluminum tubing. The probe's two arm hang downward, on either side of the measurement volume, from a supporting beam cantilevered over the fire. The distance between the outer edges of the two arms is 43 cm (17 in) (without the insulation). The vertical drop from the top of the supporting beam to the bottom surfaces

Figure 3. Insulated probe suspended over the two-meter diameter pan.

of the two arms is 76 cm (30 in). The probe, with insulation, is shown in Fig. 3 suspended above the 2 m pan.

The initial test with the probe was conducted with 23 L/min (6 gpm) of water (at ambient temperature) for cooling and two layers of ceramic cloth insulation. The insulation and cooling were inadequate, and probe temperatures of 120 °C were recorded during the test. Thus, enough insulation was added to the probe to form a 5 cm thick layer over all surfaces. A second test indicated that this insulation was adequate; the probe temperature rose only a few degrees Celsius.

A helium purge was used to keep the internal optics of the probe free of soot. Helium was chosen as the purge gas because of its relatively small refractive index. The helium was forced through the interior of the probe and exited from the two optical ports into the probe volume with a flowrate of approximately 25 slpm.

Measurements were made in a total of twelve two-meter diameter pool fires, each providing approximately four minutes of quasi-steady burning. Seven of these tests were performed at different heights (0.5 to 2.0 m in 0.25 m increments) above the fuel surface 0.1 m

Test	TDL position Height (m)	Radius (m)	Analysis Start* (s)	Length (s)	Fuel Regression (mm/min)	Initial Temp. Water (°C)	Fuel (°C)	Blowers Flow (slpm)	Temp (°C)
[6	2.03	0.51	35	270	1.6	41	34	574	33
[7	2.03	0.10	43	224	1.1	24	29	573	30
8	1.52	0.10	50	224	1.6	29	31	575	32
9	1.01	0.10	45	224	1.5	30	32	574	34
10	0.51	0.10	38	256	1.5	32	34	574	34
11	0.76	0.10	38	240	1.7	32	33	574	36
[12	1.27	0.10	30	240	1.6	32	35	574	35
[13	1.78	0.10	37	256	1.6	26	26	574	28
14	1.52	0.51	61	224	1.8	28	29	574	30
15	1.02	0.51	115	176	1.7	29	31	573	34
16	1.27	0.30	32	240	1.7	33	36	574	34
[17	1.78	0.30	44	224	–†	33	34	574	35
				Average:	1.6	31	32	574	33

* Time from ignition.

† Differential-pressure transducer data unavailable for this test.

Table 3. Operating conditions for the tests. The brackets on the left indicate which tests were run on the same day. These tests were part of a series of 18 tests conducted in August 2002. Test numbers 1–3 and 18 did not utilize the TDL probe; test numbers 4 and 5 were used to evaluate probe insulation and cooling.

from the centerline. Three tests were performed 0.5 m from the centerline at heights of 1.0, 1.5, and 2.0 m. The remaining two tests were performed 0.3 m from the centerline at heights of 1.27 and 1.78 m. Table 3 summarizes the operating conditions for the twelve tests.

The emission signals for the two tests performed 0.3 m from the centerline were unusable, probably due to misalignment in the optics. (These tests were the last two performed in this series.) Thus, only limited data from these two tests are presented.

Results

Time series data for a test performed midway through the series (height = 1.27 m, radius = 0.1 m) are shown in Fig. 4. These data are typical for this test series. The soot extinction coefficient of approximately 14 m^{-1} and the soot temperature of 1360 K compare favorably with the values measured previously by Gritzo et al. [1] in a 6 m by 6 m pool fire. Soot volume fractions shown in Fig. 4 are lower than the 2 ppm reported by Gritzo et al. Our transmission measurement gives approximately 1.14 ppm and our emission measurement

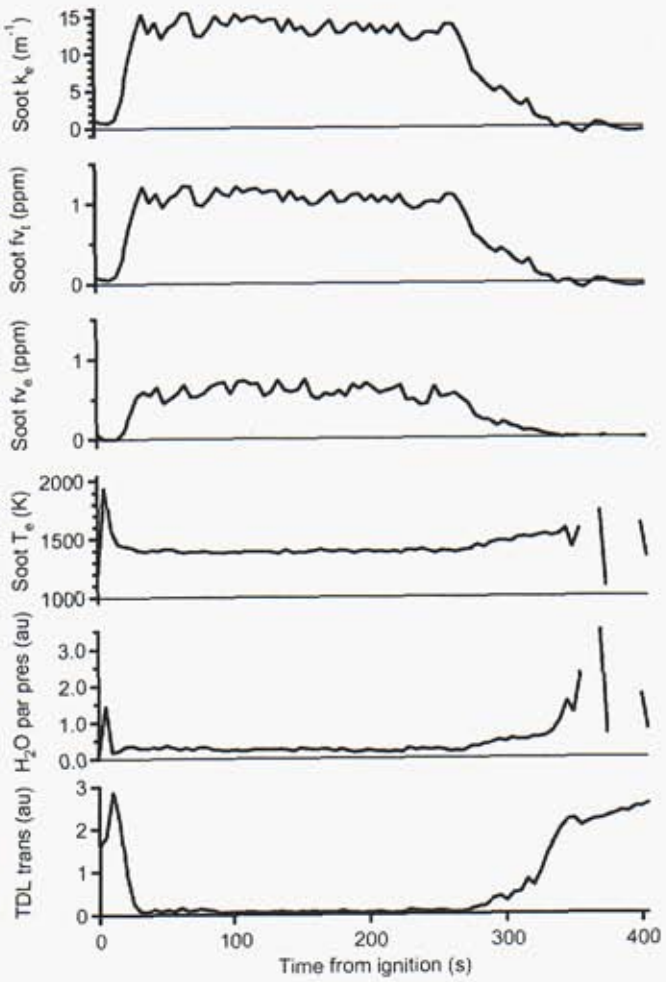

Figure 4. Time series data for a typical fire. The points shown are 5 s averages of data taken 1.27 m above the fuel surface and 0.1 m from the centerline. Discontinuities at the end of the fire in the emission-based measurements occur because the amount of emitting soot in the probe volume falls to zero as the fire burns out.

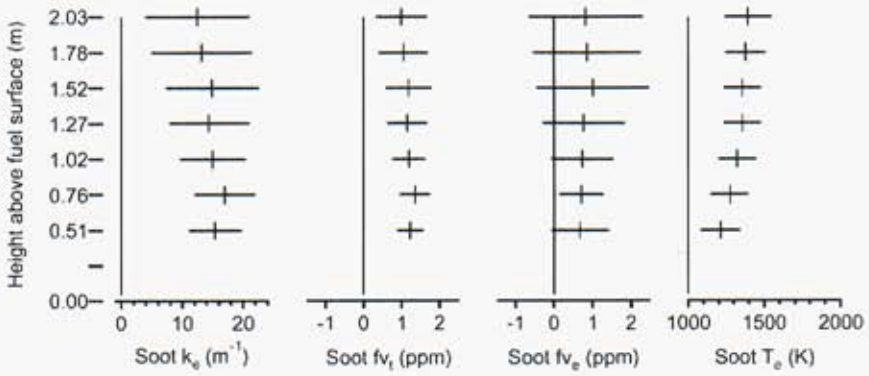

Figure 5. Measured soot properties 0.1 m from the centerline. Shown are extinction coefficient, soot volume fraction from the transmission measurement, soot volume fraction from the emission measurement, and soot temperature. The crosses indicate time-averaged values while the bars indicate the range of plus/minus one standard deviation of the measured PDF about the mean.

gives approximately 0.77 ppm. The reason for the discrepancy is our use of values for the optical constants measured in JP-8 pool fires, rather than the Dalzell and Sarofim [11] values used by Gritzo et al.

The TDL transmission (signal level received at the detector) is also shown in Fig. 4. One can see that the TDL signal almost vanishes due to soot extinction. However, there was enough signal to make a measurement. The TDL measurements of H_2O are shown in terms of partial pressure, corrected for the effects of gas density and the dependence of line strength on temperature. The H_2O partial pressure values are proportional to the actual partial pressure; absolute values are not reported due to the lack of a suitable calibration source at the time of these tests.

Soot Measurements

Figures 5 and 6 show averages and standard deviations of the soot measurements made 0.1 and 0.5 m from the centerline. The standard deviations are indicative of how broad the measured probability density function (PDF) is. The trends shown in these graphs are consistent, indicating that the fires were repeatable. This is especially true considering that the first four tests with the probe positioned 0.1 m from the centerline were done at 0.5 m increments, and then the next three tests were done at the intermediate positions.

The graphs in Fig. 5 also show that low in the flame the soot volume fraction deduced from the emission measurements is significantly lower than that determined from the transmission measurements, as has been found in other pool fire measurements [1,3]. As the measurement height increases, however, the mean emission-based and transmission-based volume fractions converge to within 20%. Uncertainties in optical constants can account for these disparities, as well as the presence of heterogeneous soot layers in the probe volume,

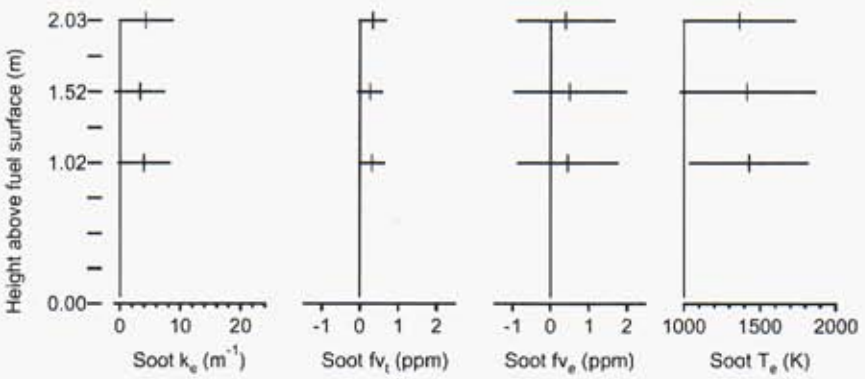

Figure 6. Measured soot properties 0.5 m from the centerline. The format and scale of the plots is the same as in Fig. 5.

as demonstrated previously in this report.

The average emission-based and transmission-based soot volume fractions in Fig. 6 also agree quite well. The large standard deviations for emission-based soot volume fraction in both figures are due to the large uncertainty inherent in that measurement. Large measurement uncertainty leads to more experimental scatter, which broadens the measured PDF. The high standard deviations are indicative of this broadening,

Probability Density Functions

Figure 7 shows probability density functions (PDFs) of soot extinction coefficient at all of the measurement locations. The measurements at 0.1 m from the centerline show the evolution of an interesting double-peaked structure. The distributions low in the fire have a strong, single peak at relatively large extinction coefficients. Measurements higher in the fire show a second peak emerging in the distribution at a lower value of the extinction coefficient.

Figures 8 and 9 show PDFs of soot volume fraction and temperature measured at 0.1 m and 0.5 m from the centerline, respectively. We see in Fig. 8 that the temperature, as well as the transmission-based soot volume fraction, shows a double-peaked structure in the distributions. As expected, the temperature distributions show a predominantly low-temperature (1210 K) peak low in the fire evolving to a predominantly high-temperature (1450 K) peak higher in the fire. The distributions measured 0.5 m from the centerline show low soot volume fractions and high temperatures, perhaps indicative of soot present in active oxidation zones.

The emission-based soot volume fraction PDFs shown in Figs. 8 and 9 are markedly different than the transmission-based distributions. At first glance, the double-peaked structure does not appear to be present in the emission measurement, although one could interpret the "peak" close to 0 ppm measured higher in the fire as a second peak. Gritzo et al. [1] also observed a double-peaked distribution for transmission-based soot volume fraction,

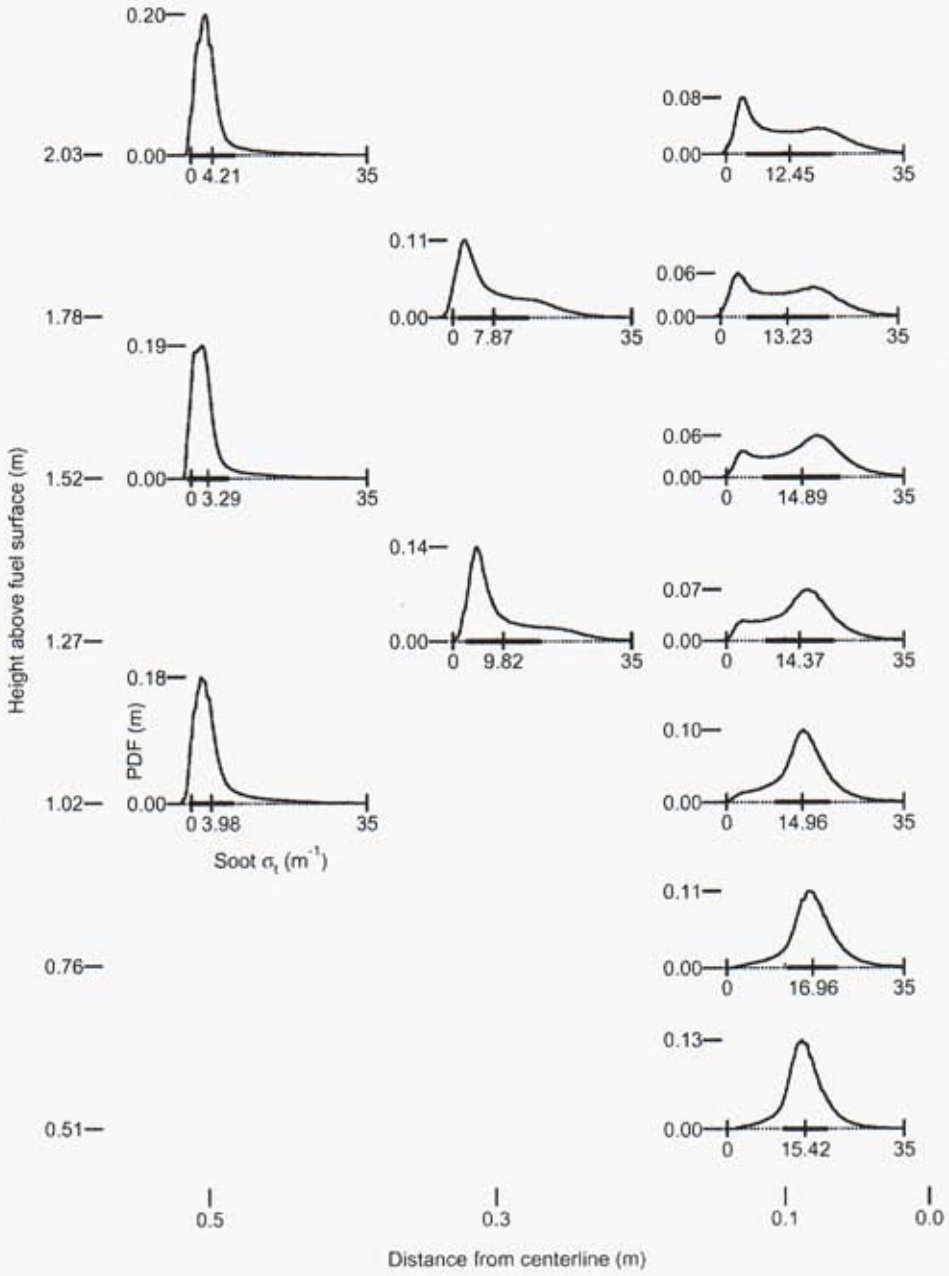

Figure 7. Extinction coefficient probability density functions (PDFs). The tick on the x-axis indicates the mean value of the PDF while the bar on the x-axis indicates the range of plus/minus one standard deviation of the PDF about the mean. The plot locations indicate the locations in the fire at which the measurements were made.

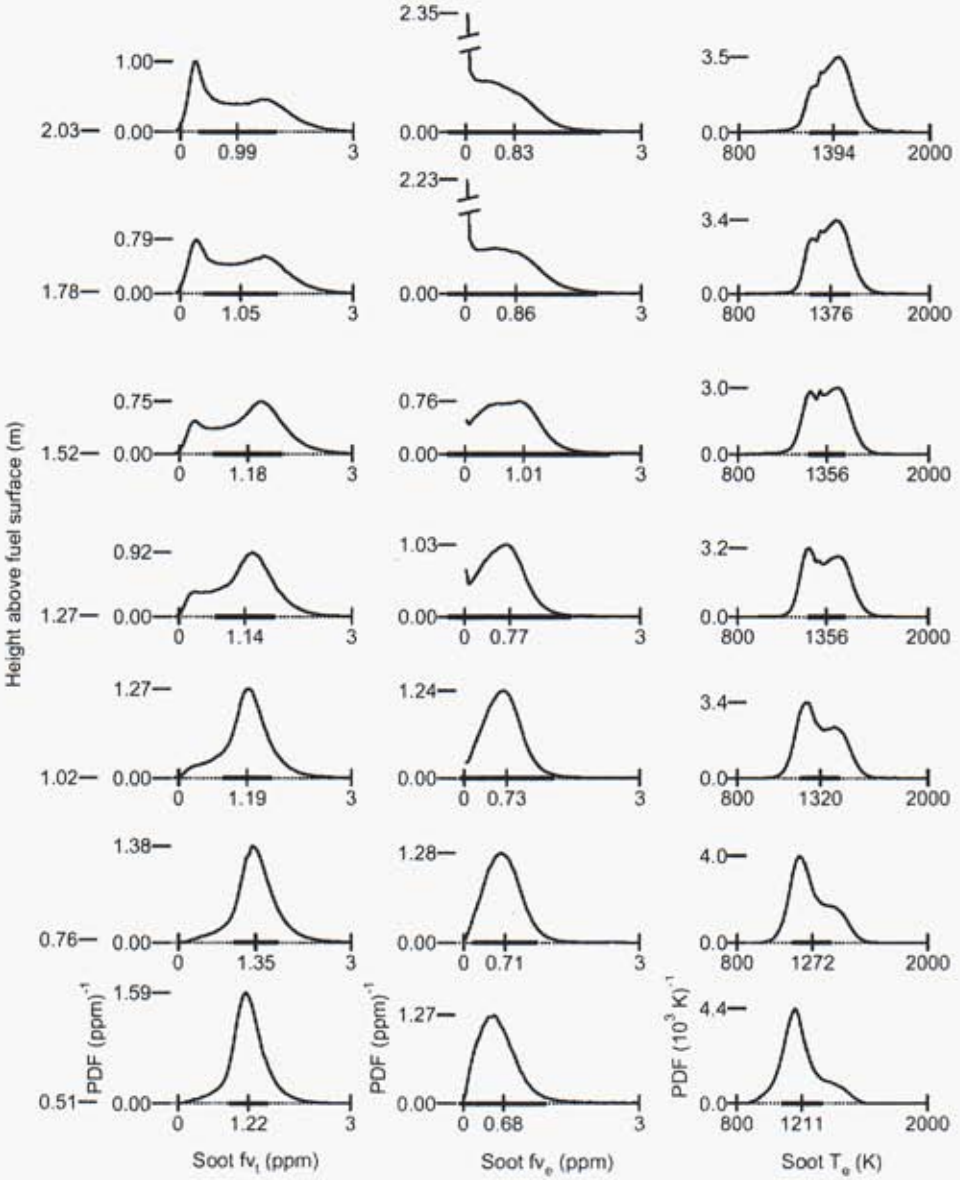

Figure 8. Soot property PDFs measured 0.1 m from the centerline. Shown are soot volume fraction from the transmission and emission measurements and soot temperature from the emission measurement. The vertical location of each plot indicates the height in the fire at which the measurements were made.

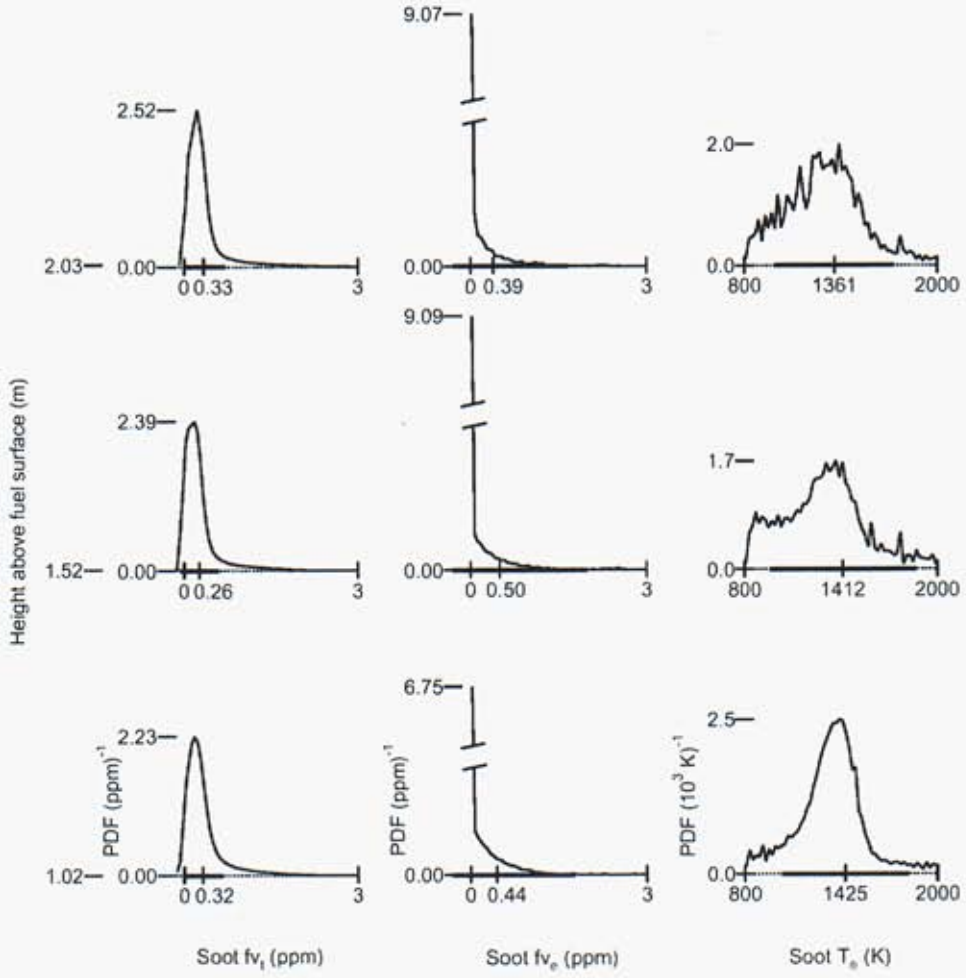

Figure 9. Soot property PDFs measured 0.5 m from the centerline.

but not for the emission-based measurement. Their explanation was that the biases in the emission measurement toward soot populations with higher temperature accounted for the discrepancy.

To examine the relationships among the different peaks in the distributions, we examine the joint-PDFs of these data, shown in Fig. 10. This figure shows that low in the fire there is a single population of relatively cold soot. As we move up in the fire, this soot tends to migrates to higher temperature and lower volume fraction (i.e., the soot occasionally undergoes oxidation). In addition, a band of soot exists at low volume fraction over a wide range of temperatures, with the temperature starting at the peak temperature (≈1500 K) and decreasing with increasing height in the flame. This population may represent the soot that underwent partial oxidation in a flame zone and then experienced thermal quenching through radiation loss and mixing with air (i.e. the smoke). At a height of 2.0 m, a significant fraction of the original soot has been oxidized and the remaining soot is either experiencing oxidation or is being quenched.

The joint-PDFs of the transmission- and emission-based soot volume fractions show that the distributions for both measurements are double-peaked at intermediate heights, and that there is a one-to-one correspondence among the peaks in the two distributions. The peaks lie above the unity line because the emission-based measurement underestimates the soot volume fraction in the probe volume due to heterogeneity.

Spectral Density Functions

Power spectral densities (PSDs) were used to examine the frequency content of the signals. Fast Fourier transforms were applied to sixteen-second blocks of data. All of the FFTs from a single experiment were then averaged together to estimate the PSD.

PSDs for the transmission-based soot volume fraction data are shown in Fig. 11. The peaks in the PSDs at the puffing frequency (0.94 Hz in these fires) are clearly visible. In some of the fires, a second peak at the first harmonic of the puffing frequency is also visible. Except at low frequencies (≈1 Hz), the PSDs calculated for different time-periods in the same fire are very consistent. Figure 12 shows a plot of the time-resolved spectra from one fire. These spectra are averages of twelve blocks of data: each block is four seconds in length. The spectral power is plotted on a linear scale in order to emphasize the differences at low frequency. The most noticeable feature is the heavy puffing at the beginning and end of the fire.

The Kolmogorov spectrum law for isotropic, homogeneous turbulence suggests that spectral power should fall off at a rate proportional to the frequency raised to the –5/3 power [30]. We estimated the frequency exponent for our data by fitting a line to the log of spectral power versus the log of frequency for different ranges of frequency. The results are shown in Fig. 13. There are distinct trends in the data with position. At low frequencies (3–30 Hz), high in the fire, the slope is approximately –1.3, which approaches the value of –7/5 (–1.4) predicted by Obukhov [31] and Bolgiano [32] for buoyancy-dominated turbulent flows. Over an intermediate range of frequencies (30–110 Hz), the values show little trend with height; all lie between –1.0 and –1.2. The PSDs transition to steeper falloffs at higher

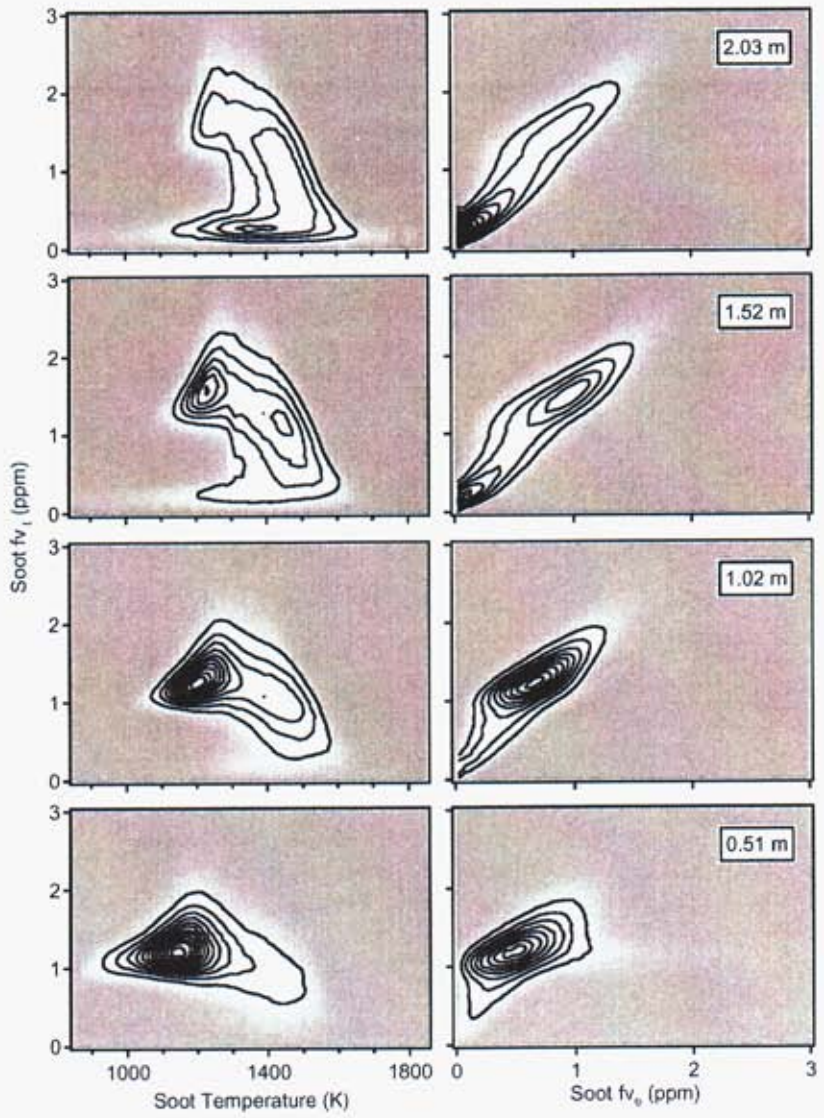

Figure 10. Joint probability density functions of soot concentration and soot temperature. These measurements were taken 0.1 m from the centerline of the fire at the heights indicated. The contour line interval is the same for all of the plots.

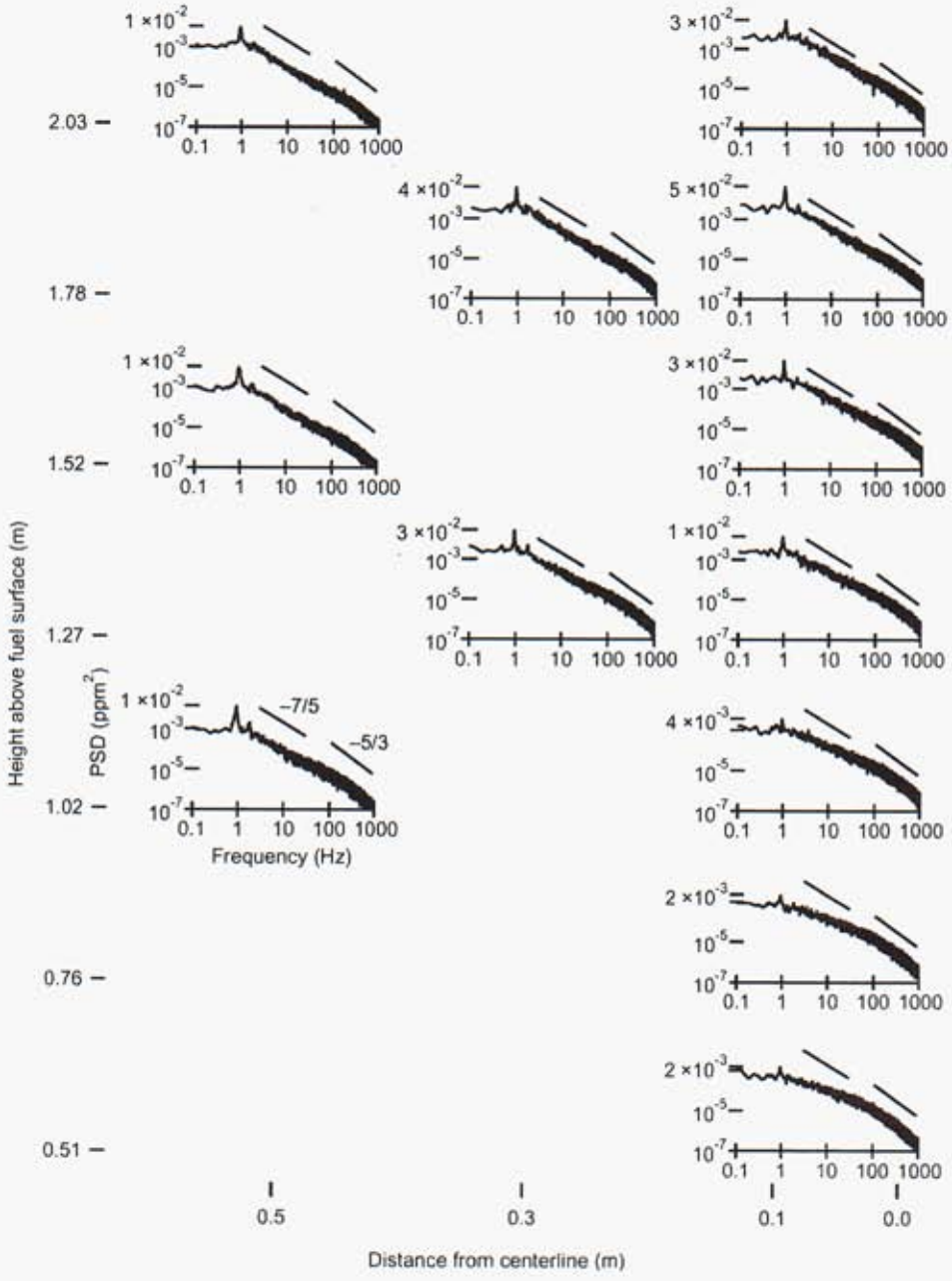

Figure 11. Soot volume fraction power spectral densities (PSDs). The two slopes show the –7/5 falloff predicted by Obukhov and Bolgiano for buoyancy-driven turbulence and the –5/3 falloff predicted by Kolmogorov for isotropic, homogeneous turbulence.

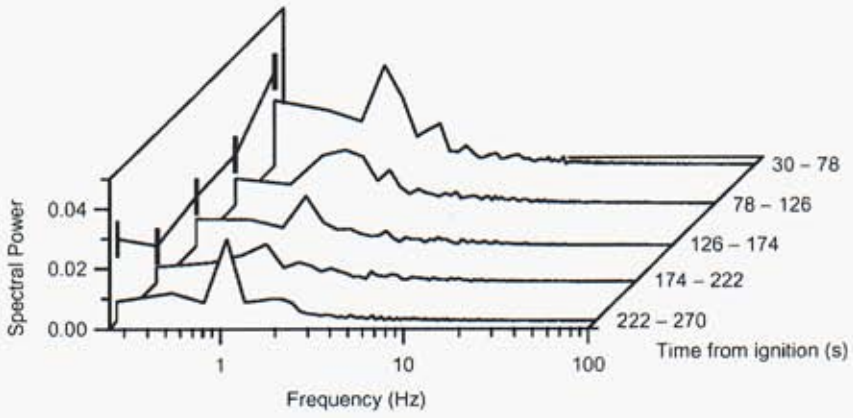

Figure 12. Waterfall plot of spectral density from the position 1.27 m above the fuel surface and 0.1 m from the centerline. The lines and markers on the left wall show the spectral power at the puffing frequency (0.94 Hz) over the time periods indicated.

frequencies (110–1000 Hz). The average slopes in this frequency range above 1 m in the fire asymptote to the –5/3 (–1.67) predicted by Kolmogorov spectrum law.

The spectral power at the puffing frequency was examined as a function of position. The results are shown in Figs. 14 and 15. The spectral power of both soot volume fraction measurements shows a very distinct trend in the data taken 0.1 m from the centerline. The puffing is very weak low in the center of the fire. Higher in the fire, the puffing gets stronger, until it peaks at 1.78 m above the fuel surface. The trend in temperature is weaker, showing a sharp break between 1.02 and 1.27 m above the fuel.

Data taken 0.5 m from the centerline, shown in Fig. 15, do not show discernable trends. The strength of the puffing is generally lower than on the centerline at similar heights in the fire.

Cross-Correlations

We calculated cross-correlation coefficients (by taking the covariance and dividing by the product of the standard deviations) among the various measured quantities. These coefficients are shown in Figs. 16 and 17. The soot volume fractions from the transmission and emission measurements show a correlation coefficient of approximately 0.3. Both soot volume fraction measurements are inversely correlated with soot temperature. This inverse correlation indicates that the larger soot volume fractions correspond to lower temperatures and vice versa. This conclusion is consistent with the interpretation of the PDFs.

Cross-spectral densities were also computed to examine correlations between soot volume fraction and temperature as a function of frequency. In particular, the phase relations among the quantities were investigated by plotting magnitude and phase of the cross-spectral density as a function of position at the puffing frequency of 0.94 Hz.

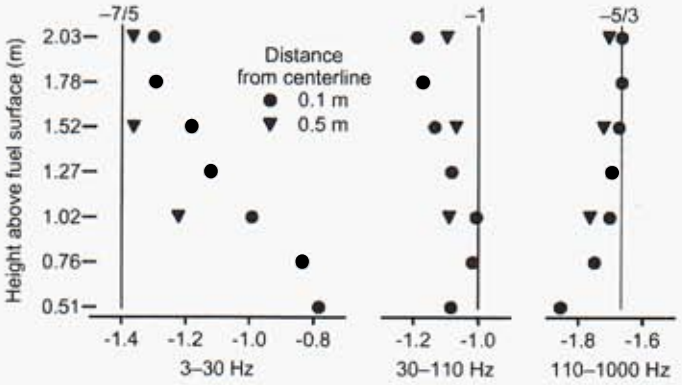

Figure 13. Frequency exponents of spectral power falloffs for different frequency ranges.

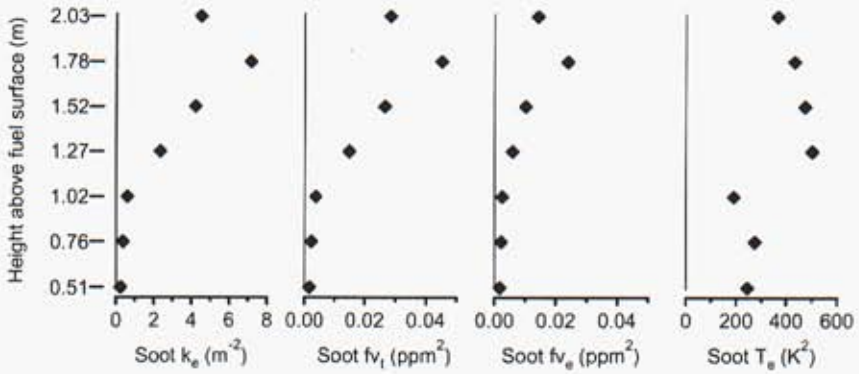

Figure 14. PSD magnitude at the puffing frequency (0.9 Hz) measured 0.1 m from the centerline.

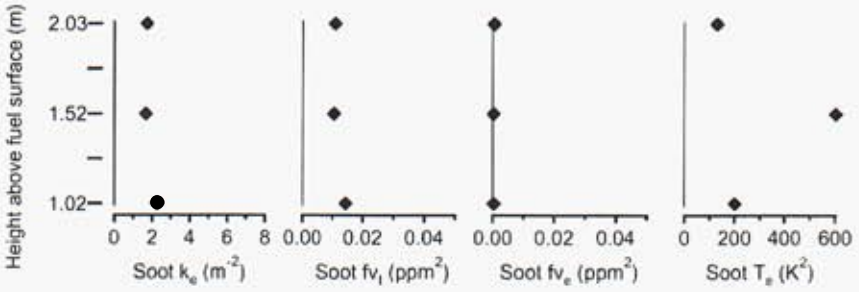

Figure 15. PSD magnitude at the puffing frequency measured 0.5 m from the centerline.

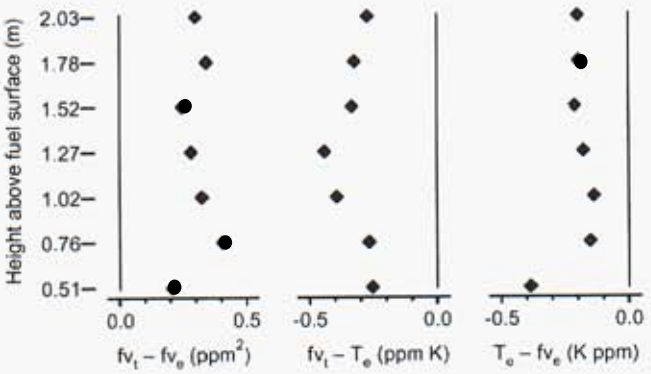

Figure 16. Correlation coefficients of measurements made 0.1 m from the centerline.

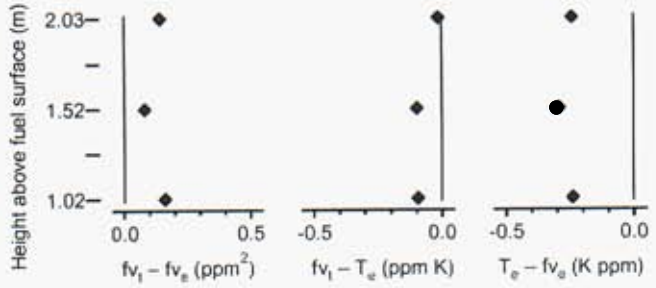

Figure 17. Correlation coefficients of measurements made 0.5 m from the centerline.

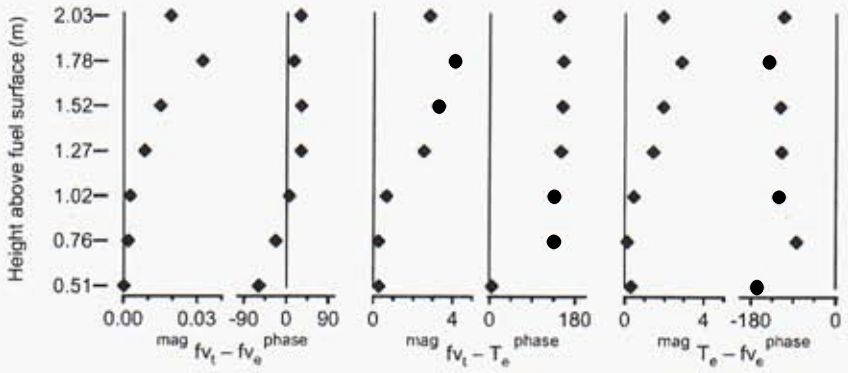

Figure 18. Cross-spectral density magnitude and phase at the puffing frequency for measurements made 0.1 m from the centerline.

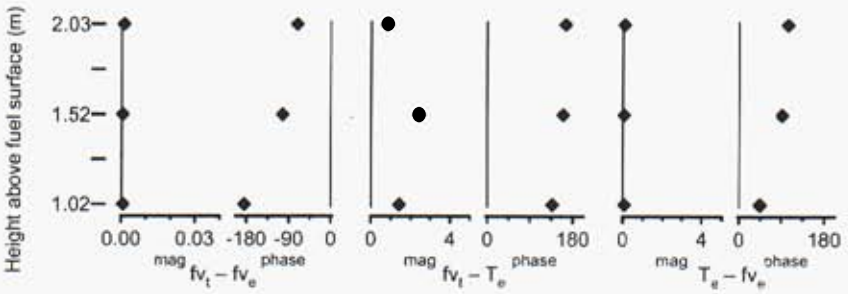

Figure 19. Cross-spectral density magnitude and phase at the puffing frequency for measurements made 0.5 m from the centerline.

The results are shown in Figs. 18 and 19. The phase relations are especially interesting. The soot volume measurements are in phase, as would be expected, high in the fire. However, these measurements are approximately 45 degrees out of phase near the fuel surface. Soot volume fraction and soot temperature are approximately 135 degrees out of phase at most locations in the fire, although they become in phase close to the fuel surface. These trends are for the most part mirrored in the measurements 0.5 m from the centerline. The exception is the two soot volume fractions, which are a full 180 degrees out of phase at the fuel surface. The magnitude of the cross-spectral density is very small at this position, however, so the large difference in phase may not be significant.

Integral Time Scales

Auto-correlations were calculated by taking the inverse Fourier transform of the power spectral density functions. Typical data are shown in Fig. 20. Positions high in the fire show the distinctive oscillations of the puffing. Positions low in the fire show little or no oscillations. The deviation of the auto-correlation for soot temperature shown in Fig. 20 at

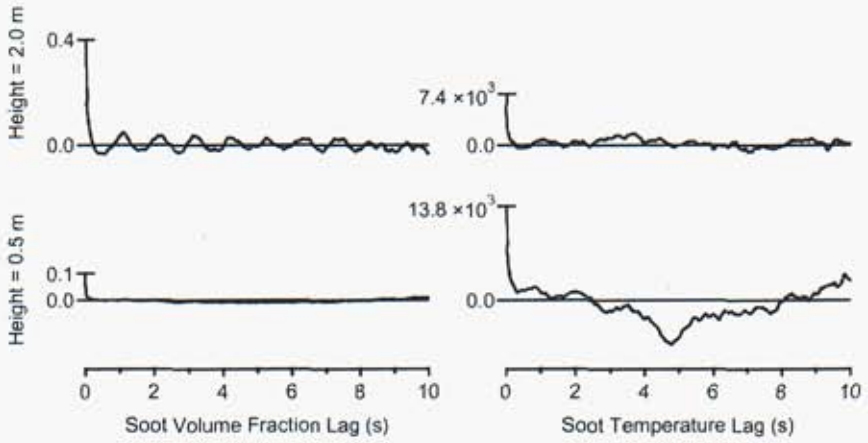

Figure 20. Auto-correlations of soot volume fraction and temperature 0.1 m from the centerline.

the 0.5 m height indicates that the mean square value of the temperature was not constant throughout the duration of the fire.

Integral time scales were estimated from the first zero-crossing of the auto-correlation functions. The measured values are shown in Fig. 21. Integral time scales for soot volume fraction (both transmission- and emission-based measurements) were between 0.2 and 0.3 s at positions higher than 1 m in the fire. These values are approximately twice the values measured by Gritzo et al. [1] for their 6 m by 6 m fire. Gritzo et al. also measured time scales for soot temperature which were significantly smaller than the time scales for soot volume fraction. That was not the case here; time scales for soot temperature were approximately the same as those for soot volume fraction at positions above 1.5 m in the fire. These results indicate that the puffing frequency is the dominant timescale in the fire, unlike the fires in Ref. [1], where the puffing was inhibited.

At positions below 1 m, the time scales estimated for the two soot volume fraction measurements diverge, with the transmission measurement scales becoming higher and the emission measurement scale becoming lower. The soot temperature time scales also become higher close to the fuel surface, although this is partly an artifact of the shifting mean square value of soot temperature noted in the first paragraph of this section.

Species Measurements

Due to the low signal-to-noise of the TDL measurement, the TDL waveforms had to be ensemble-averaged in one-half second sections before the positions of the peaks could be detected. Figure 22 shows a set of TDL waveforms ensemble-averaged over the length of one of the fires. One can see that although the H_2O signal is very clear, there is little evidence of a C_2H_2 signal, in part because of poor phase locking in the modulation/lock-in

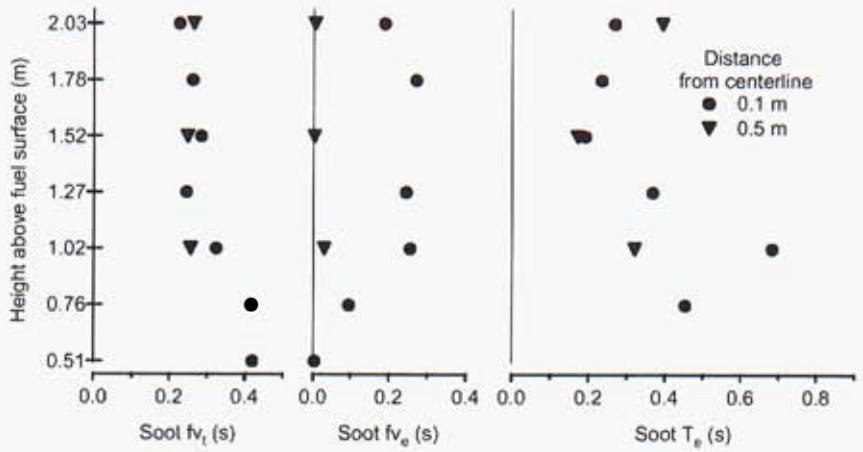

Figure 21. Integral time scales estimated from the first zero-crossing of the auto-correlation functions. Positions with a missing data-point did not have a zero-crossing in the auto-correlation at a lag of less than 1 s.

amplifier set-up. Thus, only H_2O data is presented in this section.

After ensemble averaging, the effective data rate of the TDL signals was 2 Hz. Also, since the TDL signal is proportional to the TDL 0f signal, the waveforms must be normalized by the TDL 0f signal to get actual line strength. For the data presented here, the TDL waveforms were ensemble-averaged before they were normalized. This procedure improved the signal-to-noise ratio, but effectively weighted the averages by the mean transmitted power of the TDL lasers. Since transmitted power is, in part, related to soot extinction, this weighting probably produces a bias in the statistics towards situations where there is less soot in the probe volume and therefore more transmitted power.

To reduce the effects of this possible bias on the interpretation of the data, the transmission and emission measurements were also ensemble averaged using the same weighting. The results are presented in Fig. 23. The averages shown here are slightly different than those shown in Fig. 5 because of the weighted averaging. The standard deviations are smaller because of the 2 Hz effective sample rate of these data.

Figure 23 shows that water vapor concentration is quite consistent close to the centerline, except perhaps at 2 m in height. Since water vapor indicates the presence of combustion products, one would expect the average concentration to increase with height in the fire. We lacked a calibration for water vapor, so the measurements of partial pressure are presented in arbitrary units. However, we expect the numbers presented to roughly correspond (within a factor of three) to partial pressure in bar.

Figure 24 show correlation coefficients calculated from the ensemble-averaged data. Water vapor shows a strong correlation with soot temperature and transmission-based soot concentration lower in the fire. Curiously, the emission-based measurement of soot volume fraction shows little correlation with water vapor.

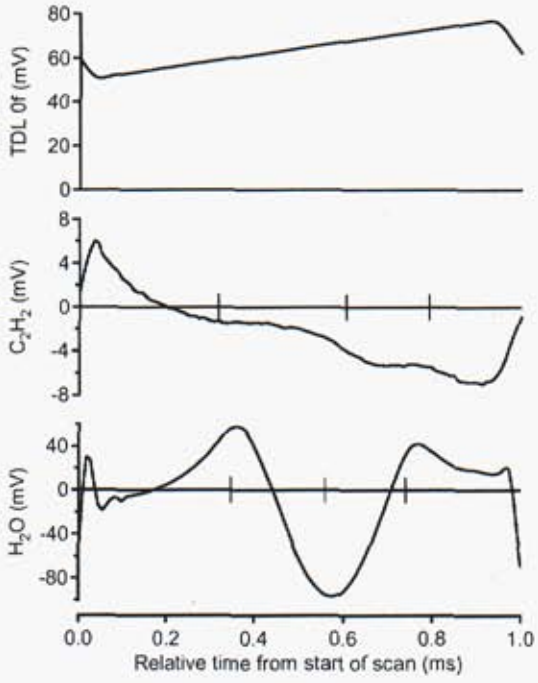

Figure 22. Typical ensemble-averaged TDL signals. These data were taken at a height of 1.27 m, 0.1 m from the centerline. The graph for H_2O shows a typical second-harmonic lineshape of a spectral adsorption feature. (Increasing time along the x-axis corresponds to increasing wavelength.)

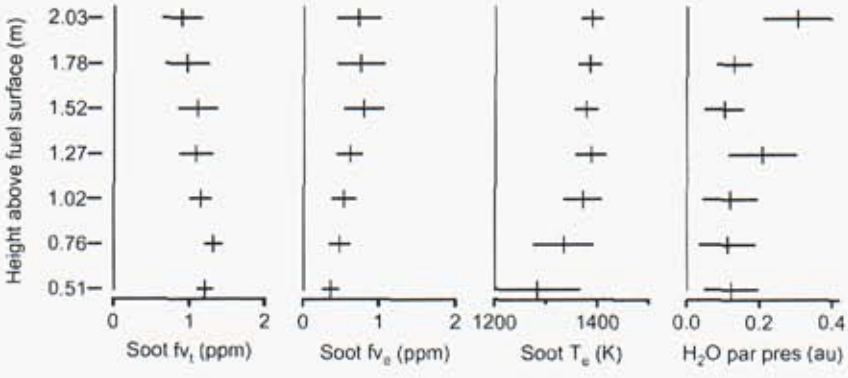

Figure 23. TDL data averages and standard deviations measured 0.1 m from the centerline. The data have an effective sample rate of 2 Hz and are weighted by the strength of the TDL 0f signal, and thus differ from those data shown in Fig. 5.

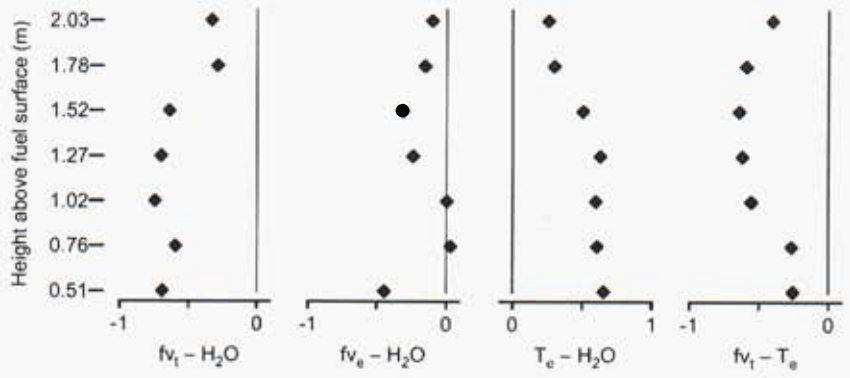

Figure 24. Correlation coefficients for the TDL data taken 0.1 m from the centerline. Water vapor shows a strong correlation with temperature low in the fire.

Conclusions

Temporally and spatial resolved in situ measurements of transmission- and emission-based soot volume fraction, temperature, and water concentration in a two-meter diameter JP-8 pool fire are reported. Distributions of soot volume fraction and temperature showed a single, predominantly low temperature peak low in the fire evolving to a predominantly high temperature, low soot volume fraction peak high in the fire. Power spectra showed a trend towards stronger puffing high in the fire. The slope of the PSDs suggested a buoyancy-driven Obukhov-Bolgiano scaling ($\omega^{-7/5}$) at frequencies between 3 and 30 Hz, and Kolmogorov scaling ($\omega^{-5/3}$) at frequencies between 110 and 1000 Hz. The soot volume fraction measurements showed moderate correlation with each other. Both soot volume fraction measurements were inversely correlated with temperature. At the puffing frequency (0.94 Hz), soot volume fraction and temperature were approximately 135 degrees out of phase. Water vapor measurements were highly correlated with temperature and transmission-based soot volume fraction, but not with emission-based soot volume fraction.

References

[1] L. A. Gritzo, Y. R. Sivathanu, and W. Gill, "Transient Measurements of Radiative Properties, Soot Volume Fraction and Soot Temperature in a Large Pool Fire," *Combustion Science and Technology*, 139(1–6):113–136 (1998).

[2] Y. R. Sivathanu and J. P. Gore, "Transient Structure and Radiation Properties of Strongly Radiating Buoyant Flames," *ASME Journal of Heat Transfer*, 114(3):659–665 (1992).

[3] M. Klassen, Y. R. Sivathanu, and J. P. Gore, "Simultaneous Emission Absorption Measurements in Toluene-Fueled Pool Flames: Mean and RMS Properties," *Combustion and Flame*, 90(1):34–44 (1992).

[4] C. R. Shaddix, S. W. Allendorf, G. L. Hubbard, D. K. Ottesen, and L. A. Gritzo, "Diode Laser Diagnostics for Gas Species and Soot in Large Pool Fires: LDRD Project Final Report," Sandia National Laboratories Report No. SAND2001–8383, June 2001.

[5] J. Henningsen and H. Simonsen, "Quantitative Wavelength-Modulation Spectroscopy Without Certified Gas Mixtures," *Applied Physics B*, 70(4):627–633 (2000).

[6] L. S. Rothman, C. P. Rinsland, A. Goldman, S. T. Massie, D. P. Edwards, J. M. Flaud, A. Perrin, C. CamyPeyret, V. Dana, J. Y. Mandin, J. Schroeder, A. McCann, R. R. Gamache, R. B. Wattson, K. Yoshino, K. V. Chance, K. W. Jucks, L. R. Brown, V. Nemtchinov, and P. Varanasi, "The HITRAN Molecular Spectroscopic Database and HAWKS (HITRAN Atmospheric Workstation): 1996 edition," *Journal of Quantitative Spectroscopy and Radiative Transfer*, 60(5):665–710 (1998).

[7] L. S. Rothman, C. Camy-Peyret, J.-M. Flaud, R. R. Gamache, D. Goorvitch, A. Goldman, R. L. Hawkins, J. Schroeder, J. E. A. Selby, and R. B. Wattson, "HITEMP, the High-Temperature Molecular Spectroscopic Database," *Journal of Quantitative Spectroscopy and Radiative Transfer*. In preparation.

[8] B. L. Upschulte and M. G. Allen, "Diode Laser Measurements of Line Strengths and Self-Broadening Parameters of Water Vapor between 300 and 1000 K near 1.3 μm," *Journal of Quantitative Spectroscopy and Radiative Transfer*, 59(6):653–670 (1998).

[9] M. Q. Brewster, *Thermal Radiative Transfer and Properties*, John Wiley & Sons, Inc., New York, NY, 1992.

[10] J. J. Murphy and C. R. Shaddix, "Influence of Scattering on Soot Temperature Measurements in Pool Fires using Optical Pyrometry," in preparation, 2003.

[11] W. H. Dalzell and A. F. Sarofim, "Optical Constants of Soot and Their Application to Heat-flux Calculations," *ASME Journal of Heat Transfer*, 91(1):100–104 (1969).

[12] K. C. Smyth and C. R. Shaddix, "The Elusive History of $\tilde{m} = 1.57 - 0.56i$ for the Refractive Index of Soot," *Combustion and Flame*, 107(3):314–320 (1996).

[13] W. L. Flower and T. M. Dyer, "Time-Resolved and Space-Resolved Measurements of Particulate Formation During Premixed Constant Volume Combustion," Sandia National Laboratories Report No. SAND79–8798, April 1980.

[14] T. M. Dyer and W. L. Flower, "A Phenomenological Description of Particulate Formation during Constant Volume Combustion," *Particulate Carbon: Formation During Combustion*, edited by D. C. Siegla and G. W. Smith, Plenum Press, New York, NY, 1981, pp. 363–389.

[15] T. P. Jenkins and R. K. Hanson, "Soot Pyrometry using Modulated Absorption / Emission," *Combustion and Flame*, 126(3):1669–1679 (2001).

[16] Ü. Ö. Köylü, "Quantitative Analysis of In Situ Optical Diagnostics for Inferring Particle / Aggregate Parameters in Flames: Implications for Soot Surface Growth and Total Emissivity," *Combustion and Flame*, 109(3):488–500 (1996).

[17] J.-S. Wu, S. S. Krishnan, and G. M. Faeth, "Refractive Indices at Visible Wavelengths of Soot Emitted from Buoyant Turbulent Diffusion Flames," *ASME Journal of Heat Transfer*, 119(2):230–237 (1997).

[18] S. S. Krishnan, K.-C. Lin, and G. M. Faeth, "Extinction and Scattering Properties of Soot Emitted from Buoyant Turbulent Diffusion Flames," *ASME Journal of Heat Transfer*, 123(2):331–339 (2001).

[19] J. Zhu, M. Y. Choi, G. W. Mulholland, and L. A. Gritzo, "Soot Scattering Measurements in the Visible and Near-Infrared Spectrum," *Proceedings of the Combustion Institute*, 28(pt. 1):439–446 (2000).

[20] J. M. Suo-Anttila and K. A. Jensen, private communication, 2003.

[21] Y. Sivathanu, A. Hamins, G. W. Mulholland, T. Kashiwagi, and R. Buch, "Characterization of Particulate from Fires Burning Silicone Fluids," *ASME Journal of Heat Transfer*, 123(6):1093–1097 (2001).

[22] G. W. Mulholland and M. Y. Choi, "Measurement of the Mass Specific Extinction Coefficient for Acetylene and Ethene Smoke Using the Large Agglomerate Optics Facility," *Twenty-seventh Symposium (International) on Combustion*, The Combustion Institute, Pittsburgh, PA, 1998, pp. 1515–1522.

[23] S. di Stasio and P. Massoli, "Influence of the Soot Property Uncertainties in Temperature and Volume-Fraction Measurements by Two-Colour Pyrometry," *Measurement Science and Technology*, 5(12):1453–1465 (1994).

[24] B. N. Taylor and C. E. Kuyatt, "Guidelines for Evaluating and Expressing the Uncertainty of NIST Measurement Results," National Institute of Standards and Technology, Technical Note 1297, Gaithersburg, MD, September 1994.

[25] P. J. Mohr and B. N. Taylor, "CODATA Recommended Values of the Fundamental Physical Constants: 1998," *Journal of Physical and Chemical Reference Data*, 28(6):1713–1852 (1999).

[26] Y. R. Sivathanu, J. P. Gore, and J. Dolinar, "Transient Scalar Properties of Strongly Radiating Jet Flames," *Combustion Science and Technology*, 76(1–3):45–66 (1991).

[27] S. R. Tieszen, T. J. O'Hern, R. W. Schefer, E. J. Weckman, and T. K. Blanchat, "Experimental Study of the Flow Field In and Around a One Meter Diameter Methane Fire," *Combustion and Flame*, 129(4):378–391 (2002).

[28] A. L. Brown and T. K. Blanchat, "A Validation Quality Heat Flux Dataset for Large Pool Fires," *Proceedings of the 2003 ASME Summer Heat Transfer Conference*, HT2003-40249, ASME, New York, NY, 2003.

[29] "Material Safety Data Sheet: JP-8 Aviation Turbine Fuel," Phillips Petroleum Company, Bartlesville, OK, June 1989.

[30] J. O. Hinze, *Turbulence*, second edition, McGraw-Hill, New York, NY, 1975.

[31] A. M. Obukhov, "On the Influence of Archimedean Forces on the Structure of the Temperature Field in Turbulent Flow," *The Reports of the USSR Academy of Sciences: Geophysics*, 125(6):1246–1248 (1959).

[32] R. Bolgiano Jr., "Turbulent Spectra in a Stably Stratified Atmosphere," *Journal of Geophysical Research*, 64(12):2226–2229 (1959).

Distribution

1 William Ciro
Dept. of Chemical and Fuels Engineering
3290 Merrill Engineering Building
50 South Central Campus Drive
The University of Utah
Salt Lake City, UT 84112-9203

1 Philip J. Smith
Dept. of Chemical and Fuels Engineering
3290 Merrill Engineering Building
50 South Central Campus Drive
The University of Utah
Salt Lake City, UT 84112-9203

1 Jennifer Spinti
Dept. of Chemical and Fuels Engineering
3290 Merrill Engineering Building
50 South Central Campus Drive
The University of Utah
Salt Lake City, UT 84112-9203

1 Elizabeth J. Weckman
Dept. of Mechanical Engineering
University of Waterloo
Waterloo, Ontario
N2L 3G1
Canada

Sandia Distribution

1	MS 9054	W. J. McLean, 8300
1	MS 9054	D. R. Hardesty, 8360
1	MS 9052	R. J. Gallagher, 8361
1	MS 9053	L. M. Pickett, 8362
1	MS 9052	L. G. Blevins, 8361
20	MS 9052	J. J. Murphy, 8361
1	MS 9052	C. R. Shaddix, 8361
1	MS 9052	T. C. Williams, 8361
1	MS 9051	A. Kerstein, 8351
1	MS 9051	R. W. Schefer, 8351
1	MS 1146	T. K. Blanchat, 9132

1	MS 1135	A. L. Brown, 9132
1	MS 1135	J. C. Hewson, 9132
1	MS 1135	K. A. Jensen, 9132
1	MS 1135	J. M. Suo-Anttila, 9132
1	MS 1135	S. R. Tieszen, 9132
1	MS 0834	S. P. Kearney, 9112
1	MS 0834	T. J. O'Hern, 9112
1	MS 0821	L. A. Gritzo, 9132
3	MS 9018	Central Technical Files, 8945-1
1	MS 0899	Technical Library, 9616
1	MS 9021	Classification Office, 8511 for Technical Library, MS 0899, 9616 DOE / OSTI via URL